# Theoretical investigation and experiment of a disc-shaped triboelectric energy harvester with a magnetic bistable mechanism

**Huai Zhao[1], Huajiang Ouyang[1*]**

[1]Faculty of Science & Engineering, School of Engineering, University of Liverpool, Liverpool, L69 3GH, UK

**Email**: H.Ouyang@liverpool.ac.uk

## Abstract

Triboelectric energy harvesting has emerged as a promising route to scavenge ambient mechanical energy for cost-effective, clean and sustainable electricity. Disc-shaped triboelectric energy harvesters are suitable for two kinds of mechanical energy sources: continuous rotation and vibration. A majority of current studies about disc-shaped triboelectric energy harvesters focus on scavenging energy in continuous rotation, but there is a lack of investigations on angular vibration, especially in structural dynamics. In this work, a new disc-shaped triboelectric energy harvester with a bistable mechanism enabled by two repulsive magnets is developed for harvesting vibration energy. There are two discs in the harvester, one stationary and the other undergoing angular oscillation. Both have segmented triboelectric films on their contact surfaces. The magnetic bistable mechanism is utilized for the first time in a disc-shaped triboelectric energy harvester for efficiency enhancement.

A comprehensive theoretical model coupling both structural dynamic and electric dynamic domains is established. A comparison between the coupled and uncoupled models reveals that the electrostatic torque between electrodes can be ignored. Numerical simulations are carried out to investigate the effect of the potential wells due to the two magnets, basins of attractors and the influence of damping from the perspective of structural dynamics. A prototype is fabricated for experimental investigations, which demonstrate that the harvester with the bistable mechanism can achieve a better performance than the corresponding harvester without the bistable mechanism, and the output voltage of the harvester increases with the increase of excitation amplitude. Theoretical and experimental comparisons about the electric outputs between the triboelectric films with different segmentation structures reveal that increasing the number of sectors on the films effectively improves the harvesting efficiency. This work establishes a link between the structural dynamics and electric dynamics for the vibration-based disc-shaped triboelectric energy harvester, providing guidelines for its design and fabrication.

Keywords: triboelectric energy harvesting, disc, angular vibration, bistable mechanism

 

## 1. Introduction

### *1.1 Triboelectric energy harvesting*

In the last few decades, renewable energy markets have been booming due to environment deterioration and gradual decrease of traditional fossil fuel. As a substitute for traditional energy supply, energy harvested from the ambient environment is a low-cost and environmentally friendly approach for generating power. Among various means of energy harvesting, triboelectric energy harvesting is a promising technology based on the coupling of triboelectrification and electrostatic induction, which can be utilized to harvest mechanical energy and generate electricity to power wearable devices and miniature sensors for monitoring structural health, environment and human beings. Since Wang's team proposed a triboelectric nanogenerator (TENG) in 2012 [1], triboelectric energy harvesting has gained much attention due to its distinct advantages, such as impressive cost-effectiveness, light weight, availability of a wide range of materials, convenience of manufacture, and high applicability [2].

According to the working mechanism of triboelectric energy harvesting, there are four basic working modes, namely vertical contact-separation mode [3,4], in-plane sliding mode [5,6], single-electrode mode [7,8] and free-standing triboelectric-layer mode [9,10]. Based on the four working modes, a variety of triboelectric energy harvesters have been developed and investigated. Among those designs, rotary discs, as a kind of advanced configuration, are usually utilized in triboelectric energy harvesting. A few studies about disc-shaped triboelectric energy harvesters are briefly reviewed here. Lin et al. [11] developed a TENG composed of two disc-shaped components with four sectors. One of the discs rotated at a constant speed and a linear relationship was found between the generated electric current and the rotating disc speed. To further explore the fundamental physics of rotary TENGs, a series of theoretical studies were carried out, in which conductor-to-dielectric type and dielectric-to-dielectric types [10], contact and non-contact modes[12,13] were investigated respectively. For boosting rotary energy harvesting efficiency, various materials and approaches were proposed and verified, such as introducing butylated melamine formaldehyde as a promising triboelectric material used in a rotary TENG [14], or integrating both positive and negative charged electrets into a rotational energy conversion system [15]. Zhang et al. [16]. tested a dual-mode rotating TENG with simultaneous output from both single-electrode mode and free-standing triboelectric-layer mode. It was found that the output of the free-standing triboelectric-layer mode could be promoted by switching on the single-electrode mode. In a study of a self-powered wind sensor [17], a disc-shaped TENG was integrated with a sensor to convert wind energy to electricity. Besides wind energy, disc-shaped triboelectric energy harvesters can also be used for harvesting wave energy. A radial-arrayed TENG was studied by experiment, in which a disc was connected with a transmission mechanism and could be driven by wave force to achieve continuous operation for long-term service [18]. Wang et al. [19] developed a tribo-induced smart window with a conjunction of a rotary freestanding sliding triboelectric nanogenerator and a polymer network liquid crystal cell, which was normally transparent and became opaque immediately under tribo-charging.

Nearly all the disc-shaped triboelectric energy harvesters mentioned above focus on scavenging energy from continuous rotation. Mechanical vibration energy, as an abundant energy source, has been extensively studied on different types of triboelectric energy harvesters. Nevertheless, for the disc-shaped triboelectric energy harvester, its application with a vibration source has rarely been studied, and there have been only several relevant studies. A disc-shaped TENG used to power a water quality sensor was studied, including a rotator disc, a stator disc and an eccentric block, which could response to the agitation of water wave [20]. Another disc-shaped TENG with a simple inertia mass was tested under hand swinging [21]. Although a small minority of studies involve disc-shaped triboelectric energy harvesters scavenging vibration energy, they are all purely experimental studies and there is not theoretical work on this type of energy harvesters. The structural dynamic response is significant for triboelectric energy harvesters since the process of electric charge flow depends on the relative motion between two distinct surfaces. Therefore, it is very important to understand and characterise the dynamic response of vibro-based rotary triboelectric energy harvesters for exploring the relationship between external excitation and electric output.

### *1.2 Bistable mechanism for efficiency enhancement*

For power boosting in triboelectric energy harvesting, a variety of methods have been reported and been investigated theoretically or experimentally, which can be categorized mainly into three aspects, namely material, electrical circuit and mechanical structure. Improving the electric properties of triboelectric materials is a direct way to enhance the efficiency of charge transferring, such as incorporating metallic oxide (ZnO) [22] or MXene ($Ti_3C_2T_x$) [23] into Polyvinylidene fluoride (PVDF), functionalizing polydimethylsiloxane (PDMS) with polystyrene (PS) and poly (pentafluorostyrene) (PPFS) via batch-fabrication compatible methods [24], and creating nano films with nanowires [25] or patterned arrays [26,27] on the contact surfaces. High impedance is a distinct

characteristic of triboelectric energy harvesting, which limits the current in the electric load. An effective approach to reduce the internal resistance and improve the output power is to utilize opposite needles enclosed in an inert atmosphere in the load circuit. It has been demonstrated that the equivalent impedance of energy harvesting circuit can be dramatically decreased by ten thousand times via the connection of the opposite needles within a triboelectric energy harvester [28]. In the structural aspect, for some traditional harvesters that exhibit linear vibration behaviour, their geometry and dimensions need to be selected carefully to match the resonant frequency with external excitation frequency. However, the ambient excitation frequency is random and varies under different operation conditions, which may result in a relatively low output [29]. In order to broaden frequency bandwidth, structural nonlinearity is usually introduced into energy harvesting systems. Among different nonlinear mechanisms, bistable mechanism, also called snap-through mechanism, has been widely exploited in the fields of vibration energy harvesting, especially in piezoelectric energy harvesting [30–32] and electromagnetic energy harvesting [33–35]. However, the bistable mechanism is not very common in triboelectric energy harvesting. One of the classical applications is a shock sensor with a combination of a buckled-beam and a triboelectric generator [36]. Cantilever beams with magnetic bistable mechanisms have also been investigated in sliding-mode triboelectric energy harvesters [37,38]. Besides, some pure experimental studies have been carried out for testing the performance of bistable triboelectric energy harvesters [39,40].

Generally speaking, there are three types of bistable mechanisms, magnetic attraction bistability, magnetic repulsion bistability and mechanical bistability [41]. Different from the linear mechanism, the bistable mechanism exhibits two distinct regimes of oscillation, namely intrawell oscillation and interwell oscillation, resulting from its double-well restoring force potential with two stable nodes and one unstable saddle point. It has an effect of steepening the displacement response, resulting in a higher velocity, which can provide much better performance in energy harvesting than the linear mechanism when the excitation frequency is much lower than the natural frequency [42]. Due to those distinct characteristics, some interesting phenomena, such as basins of attraction [43], and orbit jump [44], have been extensively investigated in piezoelectric energy harvesting and electromagnetic energy harvesting. The relevant studies about the nonlinear dynamics in triboelectric energy harvesting are fragmented. Therefore, there is still plenty of room to investigate the structural dynamics of triboelectric energy harvesters integrated with bistable mechanisms for optimization design and efficiency enhancement.

### *1.3 Objectives of this study*

In this paper, a disc-shaped triboelectric energy harvester working in sliding mode is proposed for scavenging vibration energy. Both theoretical studies and experimental investigations are carried out to explore the nonlinear dynamic behaviour and electrical performance of the harvester. This work aims to investigate the structural dynamics for a better understanding of the link between the external excitation and electric performance of the harvester, which provides guidelines for structure design, as well as strategies for efficiency enhancement. The novel contributions of this work are summarised as follows:

(1) Unlike a majority of disc-shaped triboelectric energy harvesters which are used for harvesting continuous rotation energy, the proposed harvester with nonlinear dynamics is designed for vibration energy.

(2) A comprehensive theoretical model coupling both structural dynamic and electric dynamic domains is established, addressing the research gap that most of the studies about disc-shaped triboelectric energy harvesters focus on theoretical or purely experimental work in electrical aspect.

(3) A bistable mechanism consisting of two magnets is utilized in the proposed harvester for efficiency enhancement, which has never been investigated in disc-shaped triboelectric energy harvesters before.

The outline for the rest of the paper is as follows: Section 2 gives the detailed information about the structure design of the proposed harvester and the working mechanism for sliding-mode triboelectric energy harvesting. A theoretical model of the harvester is established in Section 3, which includes a structural dynamical model and an equivalent electric model. In Section 4, a test structure for measuring magnetic dipole moments is presented. Meanwhile, a prototype of the harvester and the entire experiment system are introduced in detail. Numerical simulations are carried out to investigated the structural dynamics in Section 5. In Section 6, the experimental investigations and validation are presented. Finally, the main conclusions of this study are drawn in Section 7.

## 2. Design

The configuration of the proposed harvester is depicted in Fig.1 (a). In this design, two lightweight discs made of polymethyl methacrylate (PMMA) are in light contact with each other in the vertical plane. One of the discs is fixed with the vibration source and move with it, referred to as the stationary disc, and the other disc is able to rotate around its centre under horizontal excitation, referred to as the rotary disc. An eccentric mass is attached to the rotary disc, and a

cylindrical magnet ('movable' magnet A) is fixed on the eccentric mass. Another cylindrical magnet ('fixed' magnet B) is fixed on a L-shaped frame, which is attached to the stationary disc. Between the two magnets, there exists a magnetic repulsion.

The contact surface of the stationary disc is covered with a copper film on top of a dielectric film made of polytetrafluoroethylene (PTFE), and the rotary disc is covered with a copper film, as shown in Fig.1 (b). The metal films and the dielectric film have the same pattern, which includes several radially-arrayed sectors separated by equal-degree intervals. The detailed information for the geometry shape of the films (including the metal films and dielectric films) will be given in the next section.

Under horizontal excitation, the eccentric mass along with the rotary disc is able to swing around the disc centre, just like a pendulum. Consequently, electricity can be generated in sliding mode, whose working mechanism is illustrated in Fig.1 (c). The metal films on the two discs work as electrodes during electricity generation. In Fig.1 (c), the top metal film (attached to the rotary disc) is referred to as the top electrode, and the bottom metal film (attached to the stationary disc) is referred to as the bottom electrode. In the initial state (Fig.1 (c)-I), the two electrodes fully overlap. Because of the different electric polarities of the dielectric film and the metal films, electrons flow from the top electrode to the dielectric film, which results in net positive charges on the top electrode and net negative charges with equal density on the dielectric film. As a result, a small electric potential difference is built between the two electrodes. With the swinging of the rotary disc (Fig.1 (c)-II), the decrease in contact area brings about a higher electric potential difference due to an in-plane charge separation, which is able to drive a current flow through an external load to generate an electric potential drop that cancels the tribo-charge-induced potential. When the contact area reaches its minimum value (Fig.1 (c)-III), the electric potential difference reaches a maximum. Then, with the increase of contact area (Fig.1 (c)-IV), an opposite current flow is generated through the load circuit. The process above is a single cycle of charge transfer. During continuous excitation, an alternating current will be generated with the swinging of the rotary disc.

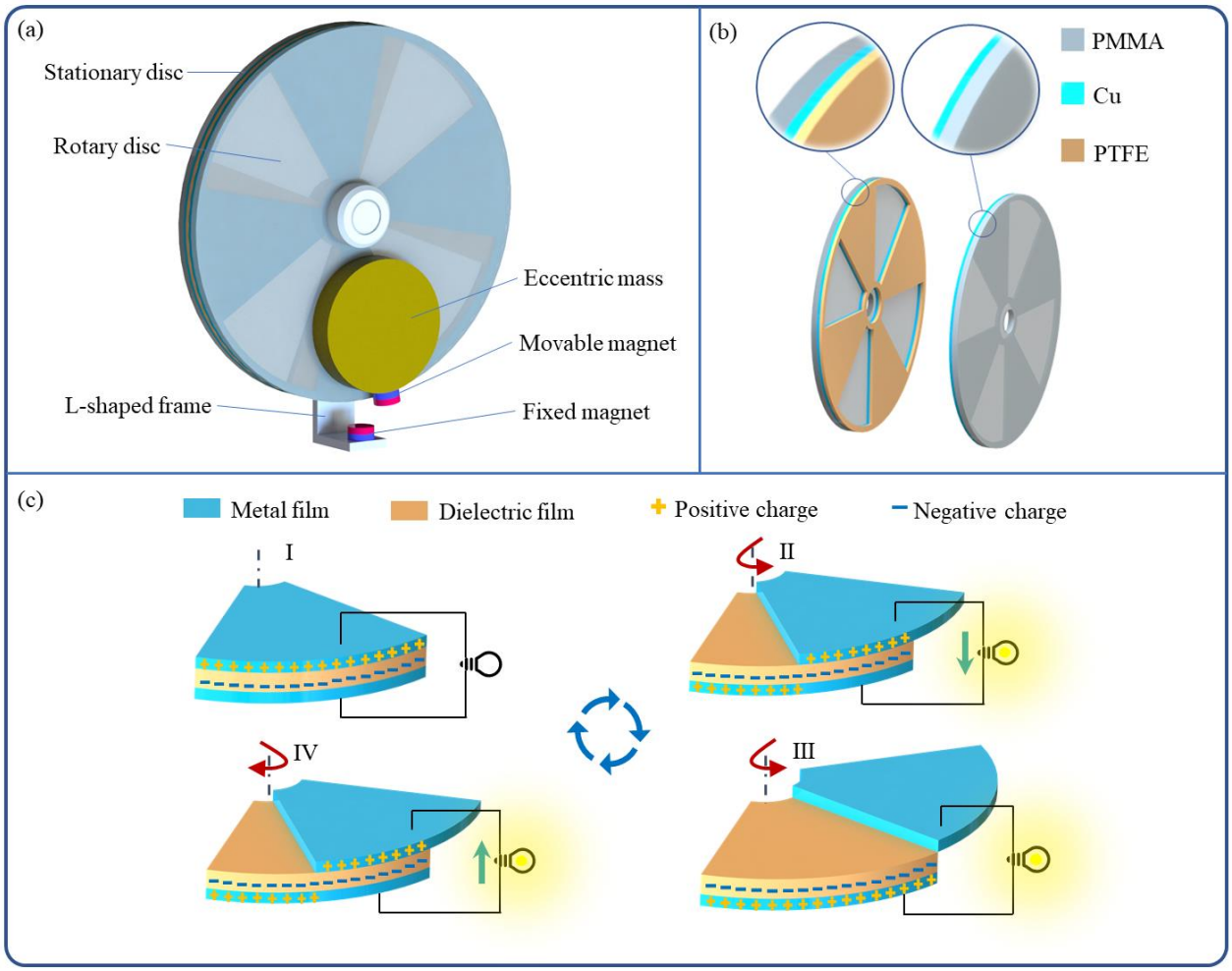


Figure 1. Configuration and working mechanism of the disc-shaped triboelectric energy harvester

## 3. Mathematical models

### *3.1 Mechanical model*

According to the configuration of the proposed harvester (Fig.2 (a)), the gravity of the eccentric mass and the magnetic force between the two magnets provide a restoring torque for the system. For the restoring torque from the gravity of eccentric mass, it can be expressed as

$$T_{\mathrm{g}} = -mgr_{\mathrm{e}}\sin(\theta) \tag{1}$$

where $m$ is the eccentric mass, including the mass of clump weight and magnet A; g is the gravitational acceleration; $r_{\mathrm{e}}$ denotes the distance between the centre of gravity of the eccentric mass and the centre of rotation; $\theta$ is the angular displacement of the rotary disc.

The restoring torque generated by magnetic force is slightly complicated due to the nonlinearity of the magnetic force. Theoretically, for two given magnets, the magnetic force depends on their relative locations, shown in Fig.2 (b). A simplified magnetic dipole model is employed, in which the magnetic force is expressed as [45,46]

$$\mathbf{F}_{\mathrm{mag}} = \frac{3\mu_0 M_{\mathrm{A}} M_{\mathrm{B}}}{4\pi r_{\mathrm{AB}}^4}[\mathbf{e}_{\mathrm{A}}\sin(\alpha) + \mathbf{e}_{\mathrm{B}}\sin(\alpha+\theta) + 2\mathbf{e}_{\mathrm{r}}\cos(\alpha) - 5\mathbf{e}_{\mathrm{r}}\sin(\alpha)\sin(\alpha+\theta)] \tag{2}$$

where $\mu_0$ is the vacuum permeability ($4\pi\times10^{-7}$ Wb/(A·m)), $M_{\mathrm{A}}$ and $M_{\mathrm{B}}$ are the magnetic dipole moment of magnet A and magnet B. $\mathbf{e}_{\mathrm{A}}$, $\mathbf{e}_{\mathrm{B}}$ and $\mathbf{e}_{\mathrm{r}}$ are the unit vectors, whose directions are illustrated in Fig.2 (b). $r_{\mathrm{AB}}$ represents the distance between the centres of the two magnets, which is expressed as

$$r_{\mathrm{AB}} = \sqrt{(r_{\mathrm{m}}\sin(\theta))^2 + r_{\mathrm{m}} + s - r_{\mathrm{m}}\cos(\theta)^2} \tag{3}$$

$\alpha$ is an angle between vector $\mathbf{e}_{\mathrm{r}}$ and the vertical dashed line, which can be obtained by

$$\alpha = \arctan\left(\frac{r_{\mathrm{m}}\sin(\theta)}{r_{\mathrm{m}} + s - r_{\mathrm{m}}\cos(\theta)}\right) \tag{4}$$

in which $r_{\mathrm{m}}$ is the distance between the centre of magnet A and the centre of rotation. $s$ denotes the gap between the centres of magnet A and magnet B when magnet A is at its lowest position.

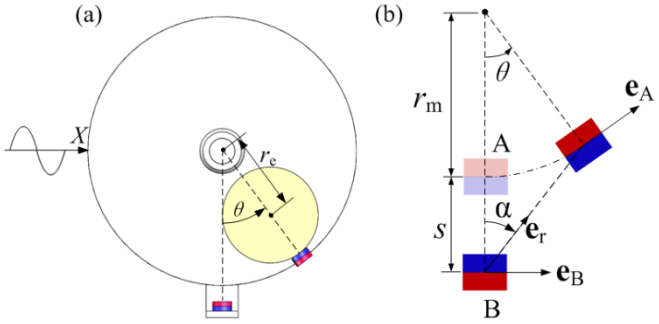


Figure 2. Schematic of structural dynamics model

According to Eq. (2), the component of the magnetic force $F_{\mathrm{m}}$ tangential to radius can be written as

$$F_{\mathrm{m}} = \frac{3\mu_0 M_{\mathrm{A}} M_{\mathrm{B}}}{4\pi r_{\mathrm{AB}}^4}[\sin(\alpha) + 3\sin(\alpha+\theta)\cos(\theta) - 5\sin(\alpha)\sin^2(\alpha+\theta)] \tag{5}$$

Therefore, the restoring torque from the magnetic force yields

$$T_{\mathrm{m}} = F_{\mathrm{m}} r_{\mathrm{m}} \tag{6}$$

By combining Eq. (1) and Eq. (6), the structural dynamic response of the harvester is governed mathematically by the following equation

$$J_0\ddot{\theta} + c\dot{\theta} + mgr_{\mathrm{e}}\sin(\theta) - F_{\mathrm{m}}r_{\mathrm{m}} = -mr_{\mathrm{e}}\ddot{X}\cos(\theta) + T_{\mathrm{e}} \tag{7}$$

where $J_0$ denotes the moment of inertia of the rotary disc and eccentric mass. $c$ is the mechanical damping under open circuit condition. $T_{\mathrm{e}}$ is the electric torque applied on the rotary disc. $X$ represents the horizontal external base excitation with a prescribed motion defined by a time function $X = A\sin(\omega t)$, in which $A$ and $\omega$ are the amplitude and circular frequency of the excitation.

### *3.2 Electric model*

Any triboelectric energy harvester can be approximately modelled by a series connection of a variable capacitance $C_{\mathrm{e}}$ and a voltage source $V_{\mathrm{oc}}$ [47]. Fig.3 (a) shows the equivalent circuit for the harvester. In this paper, the electrical model is based on the premise that the dimension of the sectors on the films is larger enough than the thickness of the dielectric film so that the edge effect between the electrodes can be ignored [47].

The equivalent capacitance $C_{\mathrm{e}}$ and the open-circuit voltage $V_{\mathrm{oc}}$ for the presented harvester can be derived as

$$C_{\mathrm{e}} = \frac{\varepsilon_0\varepsilon_{\mathrm{r}}A_1}{d_{\mathrm{t}}} \tag{8}$$

$$V_{\mathrm{oc}} = \frac{\sigma A_2 d_{\mathrm{t}}}{\varepsilon_0\varepsilon_{\mathrm{r}}A_1} \tag{9}$$

in which $\varepsilon_0$ and $\varepsilon_{\mathrm{r}}$ denote the vacuum permittivity and the relative permittivity of the dielectric film respectively. $\sigma$ represents the tribo-charge surface density and $d_{\mathrm{t}}$ is the thickness of the dielectric film. $A_1$ denotes the over-lapping area between the two metal films, and $A_2$ is the rest area of the films. Both $A_1$ and $A_2$ are functions about the rotating angle $\theta$. By introducing $\gamma = \mathrm{rem}(\theta,\ 2\beta)$, where rem (.) is a function of remainder operation, then for any arbitrary rotating angle $\theta$, $A_1$ and $A_2$ can be obtained by

$$A_1 = \begin{cases} \frac{n}{2}(\beta - |\gamma|)(r_3^2 - r_2^2) + \pi(r_2^2 - r_1^2 + r_4^2 - r_3^2), & |\gamma| \in [0,\beta] \\ \frac{n}{2}(|\gamma| - \beta)(r_3^2 - r_2^2) + \pi(r_2^2 - r_1^2 + r_4^2 - r_3^2), & |\gamma| \in (\beta, 2\beta) \end{cases} \tag{10}$$

$$A_2 = \begin{cases} \frac{n}{2}|\gamma|(r_3^2 - r_2^2), & |\gamma| \in [0,\beta] \\ \frac{n}{2}(2\beta - |\gamma|)(r_3^2 - r_2^2), & |\gamma| \in (\beta, 2\beta) \end{cases} \tag{11}$$

in which $\beta = \frac{\pi}{n}$ denotes the central angle of each sector. $r_1$, $r_2$, $r_3$ and $r_4$ are the dimension parameters of the films, which are illustrated in Fig.3 (b).

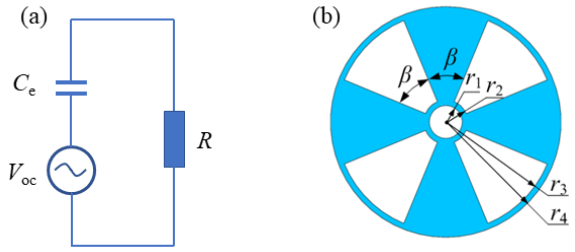


Figure 3. Equivalent electrical circuit of the harvester (a) and geometric structure of the films (b)

For a single harvester, the electricity generation equation of the harvester can be written as

$$V = -\frac{Q}{C_e} + V_{oc} \tag{12}$$

where $V$ is the voltage across the resistor $R$, and $Q$ is the amount of charge transferred in the harvester. Applying Ohm's law, one can get the electric differential equation as

$$R\frac{dQ}{dt} + \frac{Q}{C_e} - V_{oc} = 0 \tag{13}$$

The torque $T_e$ caused by the electrostatic force can be calculated by differentiating the total potential energy of the capacitive system with respect to the position of the movable electrode [48,49], which can be obtained from

$$T_e = \begin{cases} -\frac{nQ^2 d_t (r_3^2 - r_2^2)}{4\varepsilon_0 \varepsilon_r A_1^2}, \gamma \in [0, \beta] \cup (-2\beta, -\beta) \\ \frac{nQ^2 d_t (r_3^2 - r_2^2)}{4\varepsilon_0 \varepsilon_r A_1^2}, \gamma \in (-\beta, 0) \cup (\beta, 2\beta) \end{cases} \tag{17}$$

## 4. Test rig

### *4.1 Measurement of magnetic dipole moments*

A pair of identical neodymium disc magnets with a diameter of 10 mm and thickness of 3mm are used in the harvester, whose magnetic dipole moments ($M_A$ and $M_B$ in Eq. (2)) have the same value, namely $M_A = M_B = M$. To estimate the value of the magnetic dipole moment $M$, the magnetic repulsion force is measured experimentally under different gaps between the two magnets. The measurement structure is shown in Fig. 4 (a). One of the magnets is fixed on an electronic weighing scale while the other magnet is put on a movable frame of a Vernier height gauge. The magnetic repulsion force can be measured by the weighing scale, and a height gauge is utilized to adjust and measure the gap between the two magnets.

According to Eq. (2), the magnetic force between the two magnets in the measurement structure can be expressed as

$$F_m = \frac{3\mu_0 M^2}{4\pi s^4} \tag{18}$$

By adjusting the gap between the magnets, the repulsion force can be obtained at each gap. Fig.4 (b) illustrates the experimental data and the analytical result, which indicates that when the magnetic dipole moment $M$ is equal to 0.16 Wb·m, the analytical solution agrees best with the measured magnetic force.

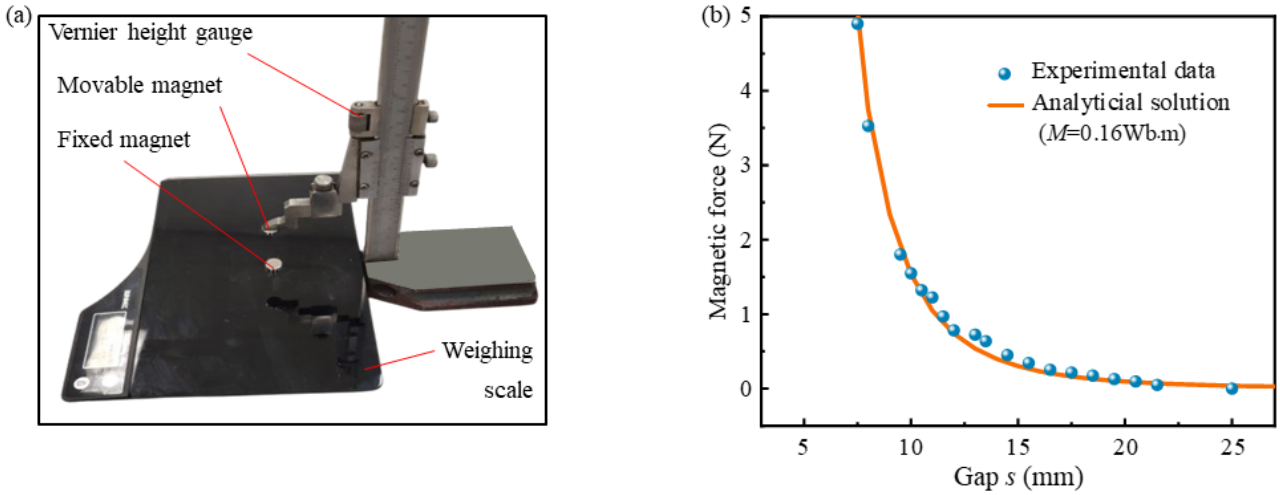


Figure 4. Measurement structure (a) and analytical solution (b)

### *4.2 Experimental system*

Based on the structure design, the proposed harvester is fabricated for laboratory testing, illustrated in Fig.5. Two transparent acrylic discs serve as substrates, covered by two copper films with a thickness of 100 μm, which are cut via a waterjet cutter. One of the copper films is then covered by a PTFE film with a thickness of 130 μm. All the films have the same pattern, including 5 equal sectors ($n$=5). An aluminium base is utilized to support the harvester. A cylindrical copper block is glued on the rotary disc serving as the eccentric mass, attached with a magnet. Another magnet is fixed on the base. The copper films (electrodes) on the stationary disc and rotary disc are wired from the edge and the centre, respectively. The corresponding design parameters of the fabricated harvester is shown in Table.1.

During testing, the protype is fixed on a shaker (APS 113), as shown in Fig.6. The BK Precision 4052 function generator and APS 125 power amplifier are employed together to power the shaker to apply excitation. An accelerometer (KISTLER 8690C50, sensitivity of 100 mV/g) is fixed on the shake table to monitor the excitation applied. A gyroscope (WT901BLEC, data output frequency: 0.1 Hz ~50 Hz; transmission distance: 50 m) is fixed on the eccentric mass to measure the dynamic response of the harvester, which is able to transmit output data to a PC via Bluetooth. Note that the mass of the gyroscope is also considered a part of the eccentric mass. The two electrodes of the harvester are wired with a load circuit including a resistor (11MΩ). In consideration of the fact that the output voltage across the load resistor may exceed the measuring range (-5 to +5 V) of the data acquisition device, the load resistor is made to consist of two smaller resistors, a resistor of 10 MΩ and another resistor of 1 MΩ, which serve as a potential divider. The voltage across the resistor of 1 MΩ is recorded. By simple mathematical conversion, the real voltage across the entire load resistor can be finally obtained. The analogue outputs of the accelerometer and the electrical output from the load circuit are processed by the NI-9234 data acquisition module and LabVIEW 2021.

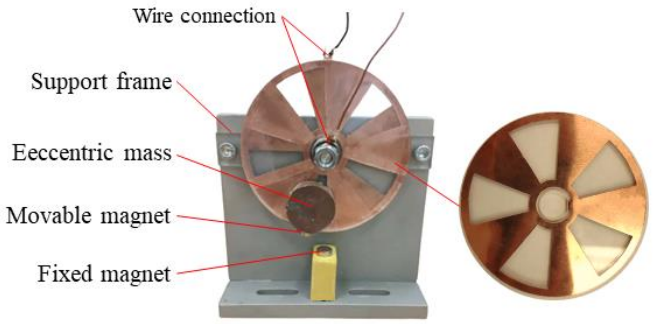


Figure 5. Prototype

Table 1. Parameters of the harvester

| Parameter | Value | Parameter | Value |
|---|---|---|---|
| $J_0$ | $1.5\times10^{-4}$ kg·m$^2$ | $r_1$ | 10 mm |
| $m$ | 91 g | $r_2$ | 14 mm |
| $r_e$ | 32 mm | $r_3$ | 46 mm |
| $r_m$ | 48.5 mm | $r_4$ | 50 mm |
| $M_A$ | 0.16 Wb·m | $\varepsilon_0$ | $8.85\times10^{-12}$ F/m |
| $M_B$ | 0.16 Wb·m | $\varepsilon_r$ | 2.05 |
| $d_t$ | 130 μm | $s$ | 12 mm |

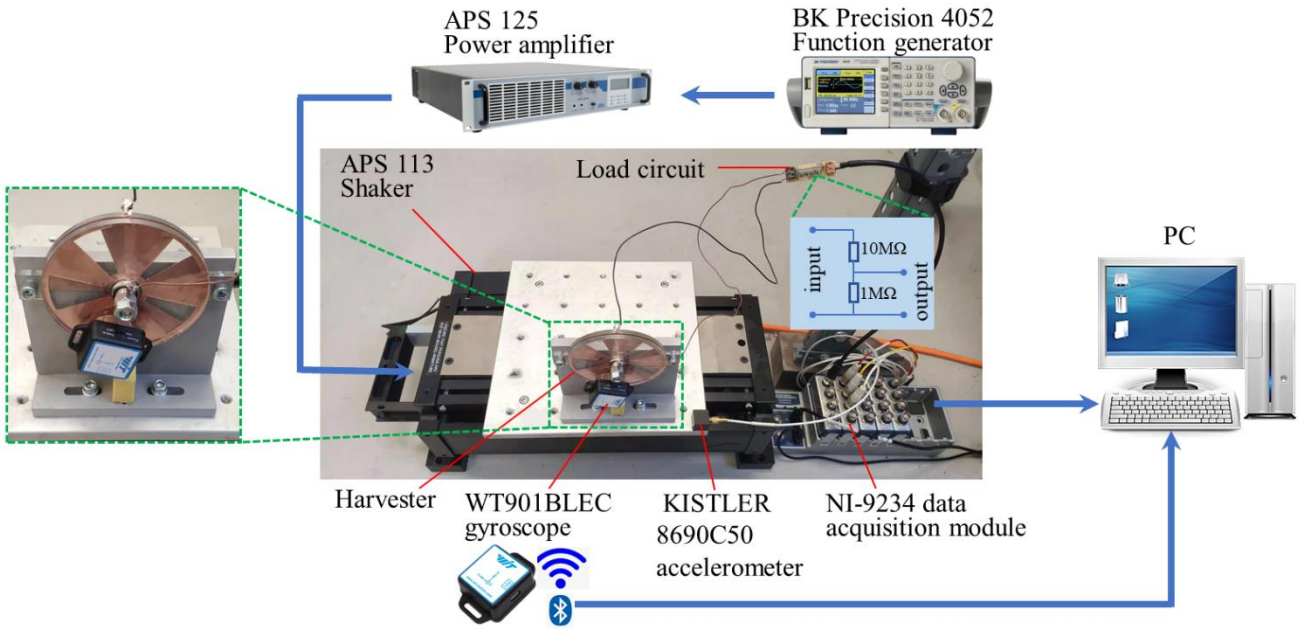


Figure 6. Experimental system

## 5. Numerical investigation on structural dynamics

### *5.1 Effect of electrostatic torque*

Due to the induced charges on the metal films and the dielectric film, there exists an electrostatic torque acting on the rotary disc. In Section 3, it can be seen that the mechanical model described by Eq. (7) and the electric model described by Eq. (13) are coupled by the electrostatic torque. The structural dynamics behaviour may be affected by the electrostatic torque, which is worthy of investigation.

A comparison between the coupled model and an uncoupled model is carried out. Note that the electrostatic torque $T_e$ in Eq. (7) should be removed in the uncoupled model. To simplify the comparison, the two magnets are not included in the two models for this particular comparison. The root-mean-square (RMS) angular displacement $\theta_{rms}$ for the eccentric mass under discrete numerical frequency sweeps (from 1 to 15 Hz) with and without consideration of the electrostatic torque (ET) is shown in Fig. 7. The charge density and damping coefficient are set as 25 μC/m$^2$ and 2×10$^{-3}$ N·m·s/rad, respectively. If the electrostatic torque has a great effect on the system, $\theta_{rms}$ is expected to be different in the two cases (with and without ET). However, Fig.8 shows that the electrostatic torque can be neglected since the RMS angular displacements are nearly the same in the two cases, which justifies decoupling of the mechanical model and the electric model. Actually, in some studies [37,50] involving structural dynamics of triboelectric energy harvesting, the force caused by the induced charges (electrostatic force) is also found to be neglectable in the mechanical system. Therefore, according to the comparison, the influence of the electrostatic torque is ignored in the subsequent analysis.

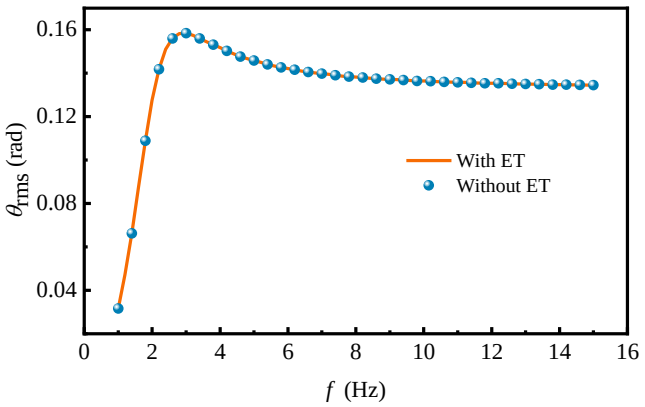


Figure 7. Comparison of the RMS angular displacements with and without the electrostatic torque

### *5.2 Influence of potential wells*

Due to the bistable mechanism, the proposed harvester has a double-well potential with two stable equilibriums and one unstable equilibrium. The corresponding potential energy and the magnetic torque in a parameter region of magnet gap $s$ and angular displacement $\theta$ are illustrated in Fig.8 (a) and (b), respectively. The two repulsive magnets with a relatively small gap introduce a high potential barrier and strong nonlinearity near the lowest position of the eccentric mass, which are weakened with the increase of the gap. This kind of mechanism is expected to broaden the frequency bandwidth of the harvester and result in higher velocities.

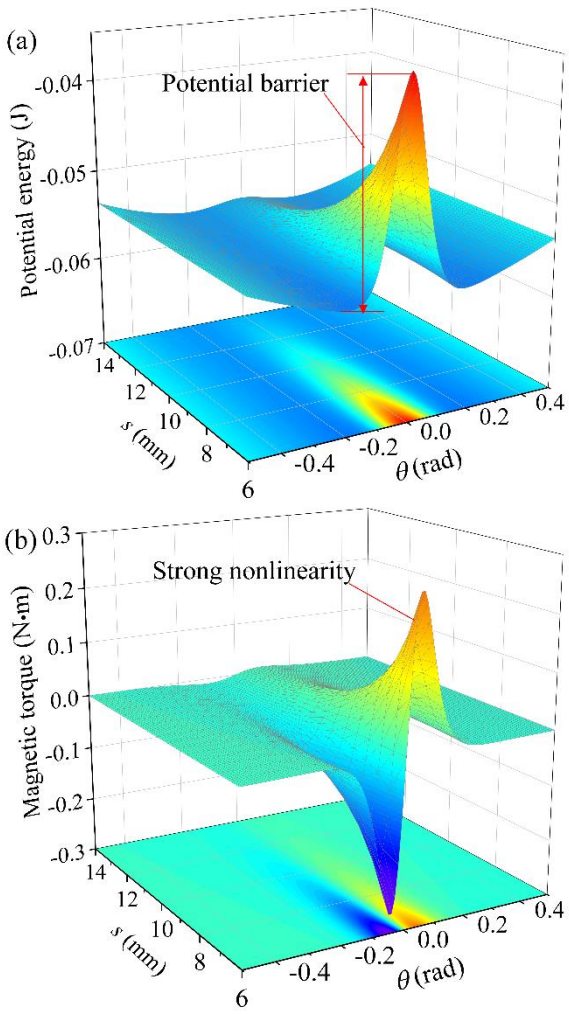


Figure 8. Potential energy (a) and magnetic torque (b) in the parameter region of gap $s$ and angular displacement $\theta$.

Fig. 9 shows the phase portraits and Fast Fourier Transform (FFT) for the angular displacement under four different gap values at $A$=0.05 m and $f$=2 Hz, where $s$=INF which means that the fixed magnet is removed. It can be seen that when the gap is relatively small, such as $s$=10 mm (Fig. 9 (a) and (b)), the eccentric mass cannot overcome the high potential barrier under the given excitation, and thus is trapped in one of the potential wells. When the gap increases to 11.2 mm (Fig. 9 (c) and (d)), due to the decrease of the potential barrier, interwell motion occurs and is accompanied with large

amplitudes. A further increase of the gap ($s$=14 mm, Fig.9 (e) and (f)) results in weak nonlinearity and the corresponding oscillation is similar to that when $s$=INF (Fig.9 (g) and (h)). As observed, the gap between the magnets directly influences the potential barrier of the system, which significantly affects the dynamic behaviour of the harvester. For further investigation of the magnet gap, a bifurcation diagram of the angular displacement $\theta$ versus the magnet gap $s$ is plotted, as shown in Fig.10, in which gap $s$ varies from 11 mm to 12 mm with an interval of $10^{-3}$ mm. Although gap $s$ varies in a small range in this figure, one-period oscillation, high-periodicity oscillation and chaos take place successively, which indicates that the system response is sensitive to the gap between the two magnets.

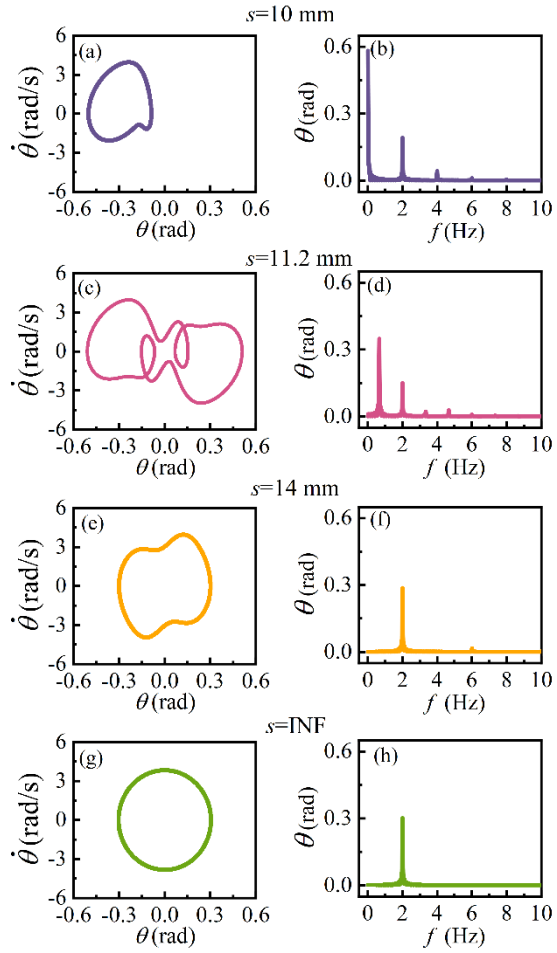


Figure 9. Dynamic response at $A$=0.05 m and $f$=2 Hz under different magnet gap $s$

It is well known that the bandwidth of energy harvesting systems can be broadened by introducing nonlinearity. Here, a linear frequency-sweeping simulation is carried out to investigate the characteristics of frequency responses of the proposed harvester. Fig.11 illustrates the frequency responses under different magnet gaps when $A$=0.01 m and $c$=2×10$^{-3}$ N·m·s/rad, in which the maximal and minimal angular displacements in steady states at each excitation frequency are marked by dots and connected via vertical lines. It is obvious that when the fixed magnet is removed ($s$=INF, Fig.11 (c)), the harvester experiences small-amplitude oscillations in the entire frequency span. When the magnet gap $s$=10 mm (Fig.11 (a)), with the increase of excitation frequency, there exist sudden jumps of the angular displacement, and large-amplitude oscillations take place in both a low frequency span (3.4 to 5.2 Hz) and a higher frequency span (7.4 to 9.0 Hz). A comparison between Fig.11 (a) and (b) indicates that a further increase of the magnet gap results in the disappearance of the large-amplitude oscillations in the higher frequency span. A detailed analysis indicates that the harvester with the magnets can achieve larger responses than the harvester without the magnets, which means that the bistable mechanism (provided by the magnets) can effectively broaden the frequency bandwidth of the harvesting system.

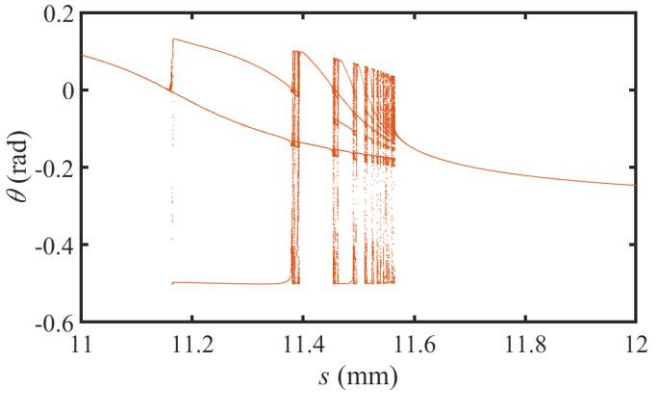


Figure 10. Bifurcation diagram of the angular displacement $\theta$ versus the magnet gap $s$ at $A$=0.05 m and $f$ =2 Hz

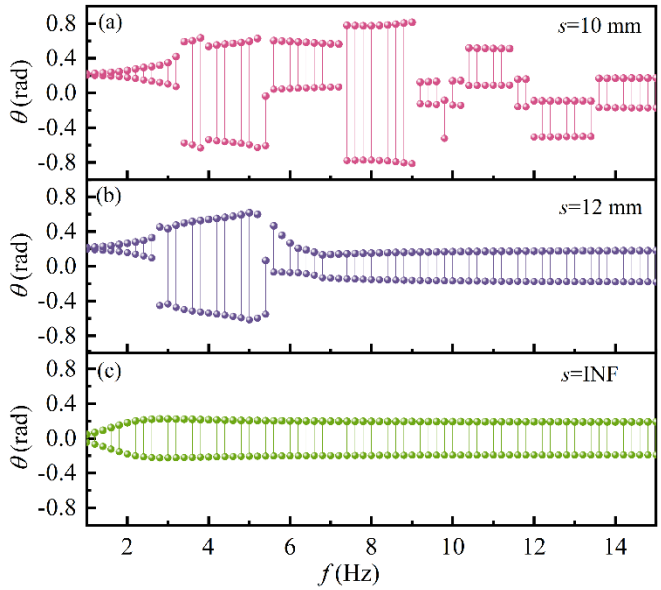


Figure 11. Frequency responses under different magnet gap $s$

### *5.3 Effect of damping*

In the proposed harvester, there exists friction between the stationary disc and the rotary disc, which is affected by the contact states between the two discs. The friction largely influences triboelectrification in triboelectric energy harvesting. On one hand, friction can enhance the charge transfer during triboelectrification. On the other hand, the mechanical energy of energy harvesting systems is dissipated by friction. The mechanism of friction in triboelectrification is out of scope of this paper, which is affected by many factors, such as chemical composition of the films, surface roughness, nature of contact, atmosphere, humidity, etc [51]. However, it is still worthy to investigate the effect of friction in structural dynamics for the proposed triboelectric energy harvester.

In this paper, in the structural dynamic model, the friction is treated as a damping term. For investigating the effect of the damping, the frequency responses of the system under different damping coefficients are studied, as shown in Fig.12, where $A$=0.01 m and $s$=10 mm are utilized. In Fig.12 (a), when the damping coefficient is relatively small, interwell oscillations with large amplitudes take place under low frequencies. A slight increase of the damping brings about the disappearance of large-amplitude interwell oscillations under low frequencies (Fig.12 (b)). Additionally, it causes interwell oscillations with small amplitudes under high frequencies (such as 12 to 13.8 Hz). In Fig 12 (c), a relatively large damping is employed, which brings about intrawell oscillations in the entire frequency span. It indicates that it is less likely for the bistable system to overcome its potential barrier under large damping.

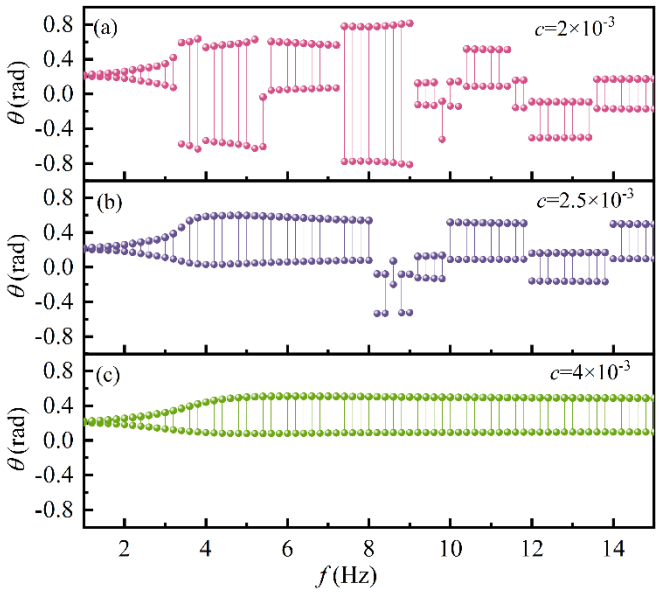


Figure 12. Frequency responses under different damping

Fig. 13 illustrates further results about the effect of the damping in a bifurcation diagram of the angular displacement versus the damping coefficient at $A$=0.01 m and $f$ =4 Hz. By combining it with Fig.12, it can be seen that interwell motion and high-periodicity oscillation are more likely to take place under low damping, while large damping may result in intrawell oscillation with one period.

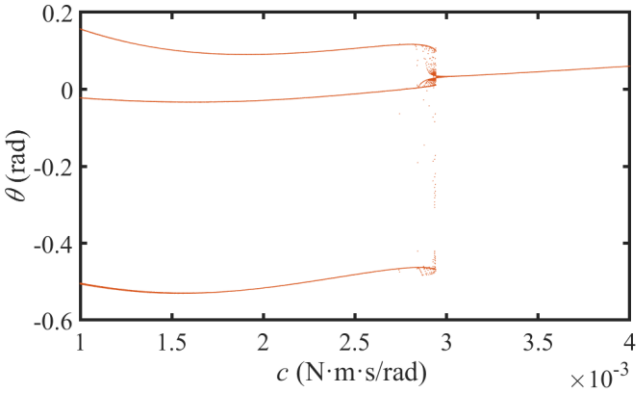


Figure 13. Bifurcation diagram of the angular displacement $\theta$ versus the damping coefficient at $A$=0.01 m and $f$ =4 Hz

### *5.4 Basins of attraction*

As the structural dynamic responses of the harvester with the magnetic bistable mechanism can be sensitive to the initial conditions, basins of attraction are investigated for further understanding the influence of the initial conditions on the structural dynamic behaviour. A series of initial conditions $(\theta_0, \dot{\theta}_0)$ are utilized in simulation, in which initial position $\theta_0$ and initial velocity $\dot{\theta}_0$ range from -3 rad to 3 rad and from -50 rad/s to 50 rad/s, respectively. According to the attractors onto which the system eventually settles down, the attractors are categorized into three types here, namely intrawell motion on the left, intrawell motion on the right and interwell motion. The steady-state responses of the system at each specific initial condition is recorded and marked with the corresponding colour according to the type of the resulting attractors.

Fig.14 illustrates the basins of attraction under four different cases, namely, case 1: $A$=0.01 m, $f$=5 Hz, $s$=8 mm; case 2: $A$=0.01 m, $f$=5 Hz, $s$=10 mm; case 3: $A$=0.03 m, $f$=2 Hz, $s$=10 mm; case 4: $A$=0.03 m, $f$=2.5 Hz, $s$=10 mm. In Fig.14 (a), it can be seen that only pure intrawell oscillations on the left side and the right side take place. The comparison between case 1 (Fig.14 (a)) and case 2 (Fig.14 (b)) indicates that with the increase of gap distance between magnets, interwell oscillations appear due to the weakened magnetic repulsion, and the three types of attractors seem to intermingle. The basin in case 3 (Fig.14 (c)) is similar to that in case 1, where no interwell oscillation occurs. In case 4 (Fig.14 (d)), at a higher

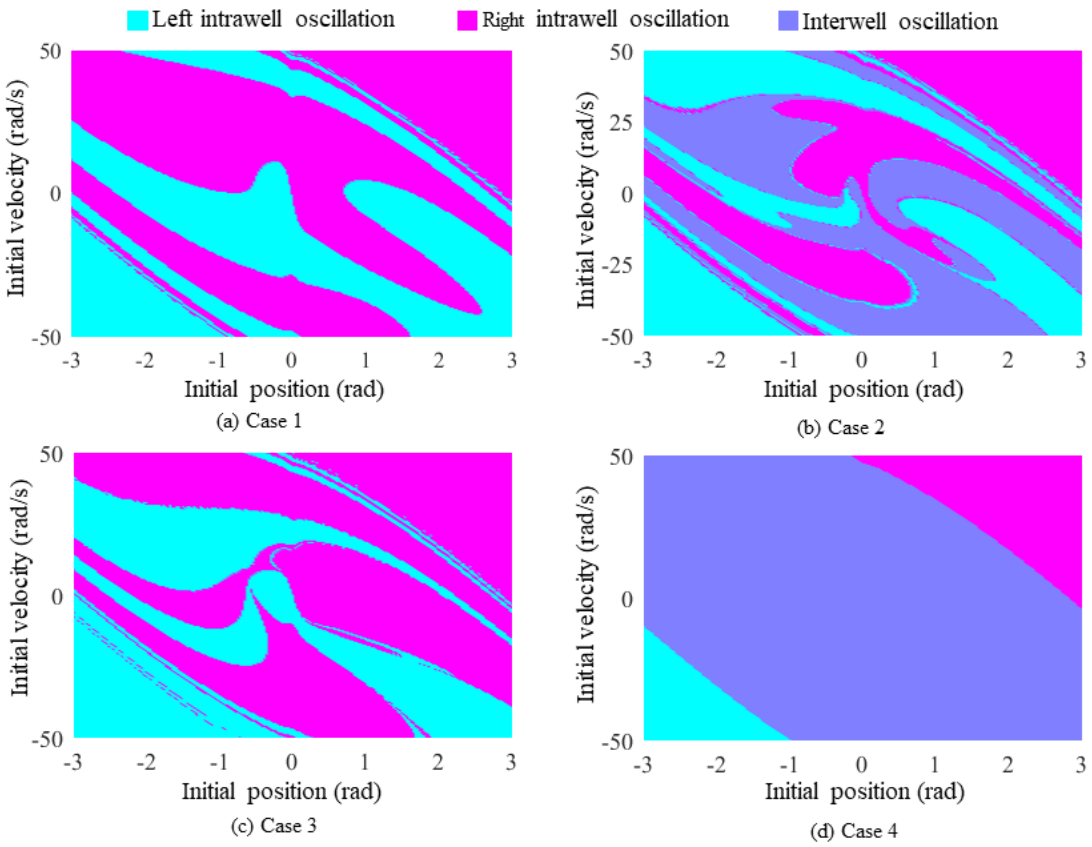


Figure 14. Basins of attractions

frequency, the basin exhibits a simple pattern, which means that the system becomes less sensitive to the initial conditions. Comparison between case 3 and case 4 indicates that a slight change in excitation level may bring about a distinct basin of attraction. The analysis above shows that the system sensitivity to the initial conditions is greatly affected by the excitation and the gap between the magnets.

## 6. Experimental work and analysis

### *6.1 Excitation level*

For assessing the electric performance of the harvester in different operation conditions, the structural responses of the eccentric mass and the voltage across the load resistor are measured under different excitation levels. Fig.15 shows an example where an excitation with an amplitude of 0.01 m and a frequency of 4 Hz is employed. The figures in the left column illustrate the angular displacement and output voltage measured in the experiments. An estimated damping coefficient ($12\times10^{-3}$ N·m·s/rad) and charge density (20 μC) are utilized in the theoretical model to match with the experimental results. The corresponding simulation results are shown in the figures in the right column. Fig.16 (a) and (b) show the measured voltage and peak power under different excitation frequencies when $A$=0.01 m. At 8 Hz, a peak power of 3.6 μW is achieved.

In order to validate the enhancement effect of the bistable mechanism, the harvesters with and without the bistable mechanism are compared experimentally, and the RMS values of the voltage across the load resistor are shown in Fig.16 (c), in which $A$=0.01 m and $s$=12 mm are used. It is obvious that the harvester with the bistable mechanism can achieve a higher output voltage than the harvester without the bistable mechanism. Actually, it is well known that bistable mechanisms are able to increase the velocity of energy harvesting systems [29]. And a higher velocity is beneficial to enhance the output performance of disc-shaped triboelectric energy harvesters. A relevant experimental study also showed that in continuous rotation, a linear relationship is found between the output current and the rotating speed of a disc-shaped triboelectric energy harvester [11].

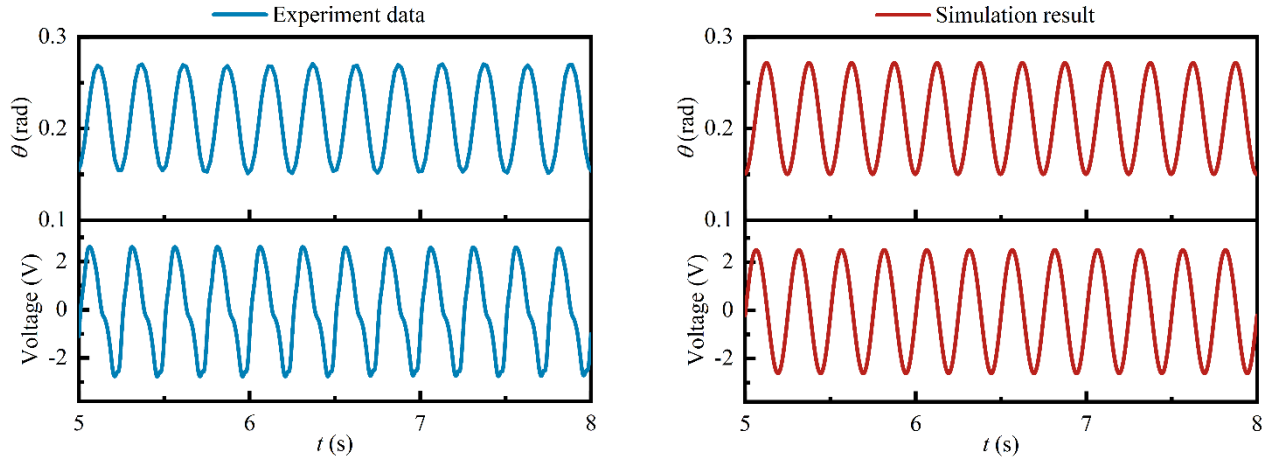


Figure 15. Experimental and simulation results at $A$=0.01m and $f$=4Hz

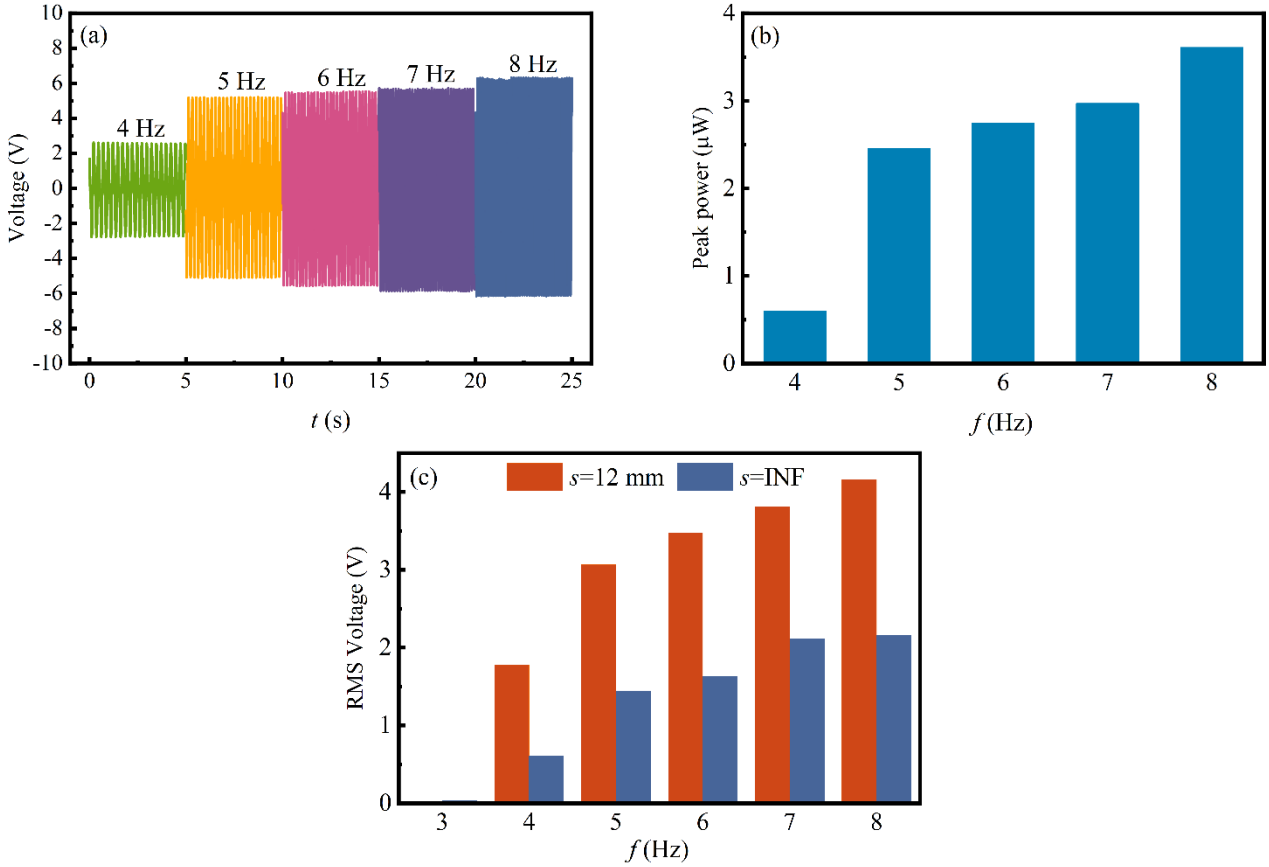


Figure 16. Measured voltage (a) and peak power (b) under different frequencies; and comparison between the harvesters with and without the bistable mechanism (c)

Under a given excitation, the excitation amplitude becomes a significant factor which largely affects the behaviour of energy harvesting systems. Fig.17 (a) and (b) show the measured voltage and peak power under different excitation amplitudes at $f$=2 Hz. With a relatively small amplitude (0.02 m), due to the weak excitation, the output voltage is very low, which obviously increases when the amplitude reaches 0.03 m. When amplitude is 0.06 m, the peak value of the measured voltage and the peak power reach 9.7 V and 8.6 μW, respectively. As observed, increasing the amplitude effectively improves the output performance.

During the comparison between the theoretical and experimental results, it is found that the damping and charge density vary with the excitation amplitude, which means that it is impossible for the theoretical model to match the experimental results when utilizing a constant damping coefficient and a constant charge density. Therefore, the damping coefficient and charge density under different

amplitudes are estimated according to the experimental results, shown in Fig.18 (a) and (b), respectively. Then those data are processed in Origin 2021, in which the nonlinear curve fitting is employed. The relationships between the damping coefficient and the amplitude, and between the charge density and the amplitude are shown in the corresponding figures. It can be seen that the damping coefficient decreases with the increase of the amplitude, while the charge density has the opposite tendency. One of the reasons causing the varying damping is believed to be the friction. Many classical studies [52,53] have proved that for contact between solid surfaces in dry conditions, kinetic friction asymptotically decreases to a constant level as the relative velocity increases. Another reason is likely the tiny and unevenness gap between the stationary disc and rotary disc due to the error of manufacturing and assembly. With the curve fitting results, the damping coefficient and charge density are modified in the theoretical model. The RMS values of the corresponding simulation results and experimental results are illustrated in Fig.18 (c), which shows good agreement.

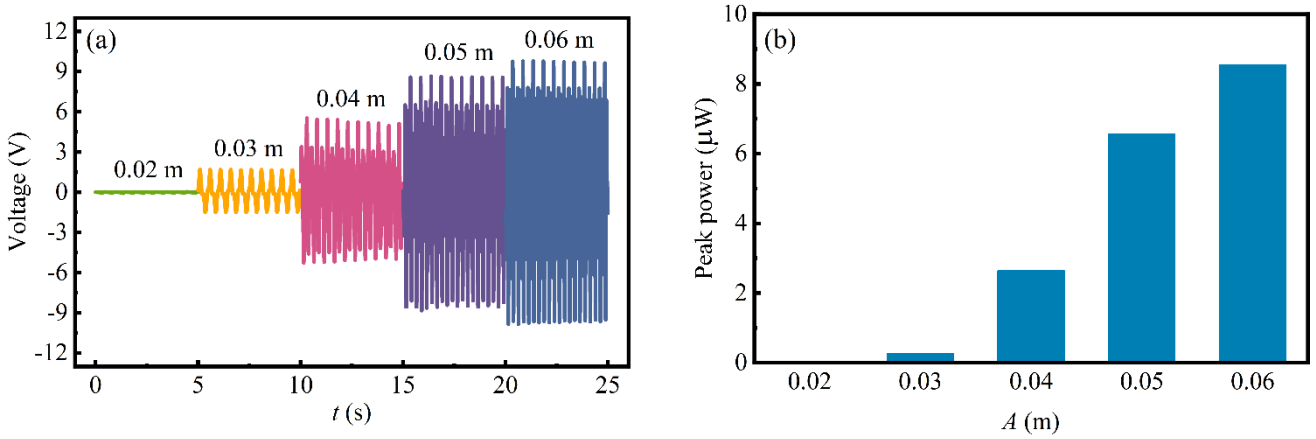


Figure 17. Measured voltage and power under different amplitudes

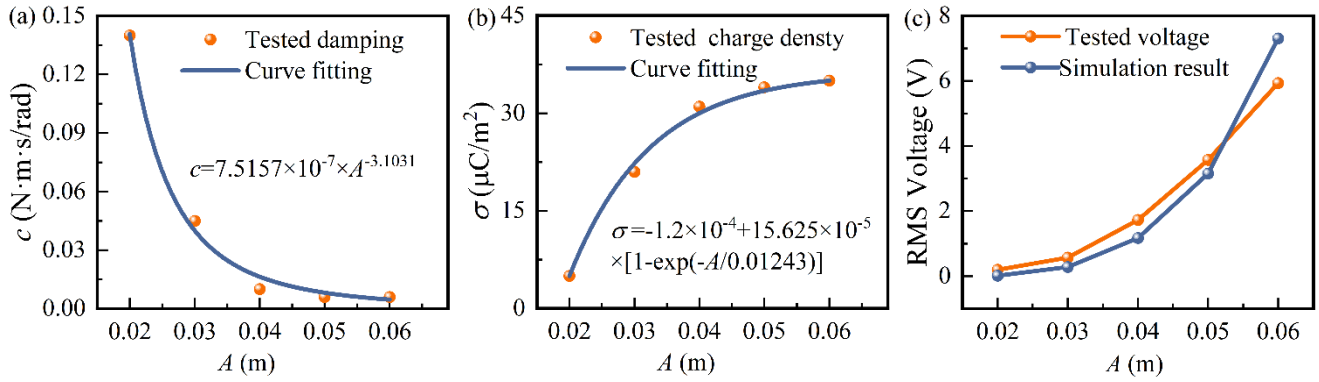


Figure 18. Curve fitting and result comparison

### *6.2 Number of sectors*

The number of the sectors on the films has a direct impact on the output characteristics of the harvester. Even under the same structural dynamic response, different segmentation structures can lead to distinct electric dynamic behaviours. From Eq. (8) to Eq. (11) in section 3.2, it can be seen that the number of sectors affects the overlapping area $A_1$, consequently the equivalent capacitance $C_e$ and the open-circuit voltage $V_{oc}$. For the triboelectric films (the copper films and the PTFE film) with $n$ sectors, increasing the number of sectors actually does not change the total effective area of the films, as well as the maximal and minimal values of the overlapping area, but it can reduce the central angle of each sector.

In order to explore the effect of the number of sectors, the overlapping area and the open-circuit voltage are studied under three different segmentation structures ($n$=5, 8 and 10) at a certain excitation ($A$=0.05 m and $f$=2 Hz), illustrated in Fig.19 (a) and (b), respectively, in which $c$=5×10$^{-3}$ N·m·s/rad, $s$=12 mm and $\sigma$=31 μC are utilized. It can be observed that when the number of the sectors $n$ is relatively small (such as $n$=5), the overlapping area just varies between its maximum value and a certain value, which is larger than its minimum

value. This means that the triboelectric films are not fully utilized during charge transfer. When $n$=8, the overlapping area varies in a wider range with a higher open-circuit voltage, but the former still does not reach its minimal value. When $n$=10, the overlapping area changes between its maximal and minimal values and more peaks appear, accompanied by an even higher open-circuit voltage with a higher varying frequency. Fig.19 (c) and (d) show the RMS open-circuit voltage, RMS current and average power under different numbers of the sectors. Obviously, the open-circuit voltage, the current across the load resistor and the output power can be effectively improved by increasing the number of the sectors on the triboelectric films, which is expected to enhance the electric performance of the proposed harvester.

To verify the enhancement effect of increasing the number of sectors, the comparison test is carried out between the films with 5 sectors and 10 sectors. Fig.20 (a) and (b) show the time histories of the measured voltage across the load resistor when $n$=5 and $n$=10 at $A$=0.05 m and $f$=2Hz, respectively. As observed, the output voltage of the harvester with 10 sectors has more peaks in the same time intervals (such as from 5.3 to 5.5s), which means that it has a higher frequency. Fig.20 (c) illustrates the RMS voltage values with the two different segmentation structures under different amplitudes at $f$=2 Hz, in which the films with 10 sectors achieve higher RMS voltage than the films with 5 sectors. Therefore, it can be concluded that the efficiency of the disc-shaped triboelectric energy harvester can be improved effectively by increasing the number of sectors on the triboelectric films. Nevertheless, this does not mean that the power of the harvester always can be improved by increasing the number of the sectors. When the number of the sectors exceeds a fairly large value, each sector becomes very narrow, and the edge effect between the two electrodes cannot be neglected any more. Once the edge effect becomes obvious, a further increase of the number of the sectors leads to a slight decrease of power output. In principle, there exists an optimal value for the number of the sectors. The edge effect is beyond the scope of this paper, and a relevant study of this matter of a different energy harvester can be seen in Ref. [47].

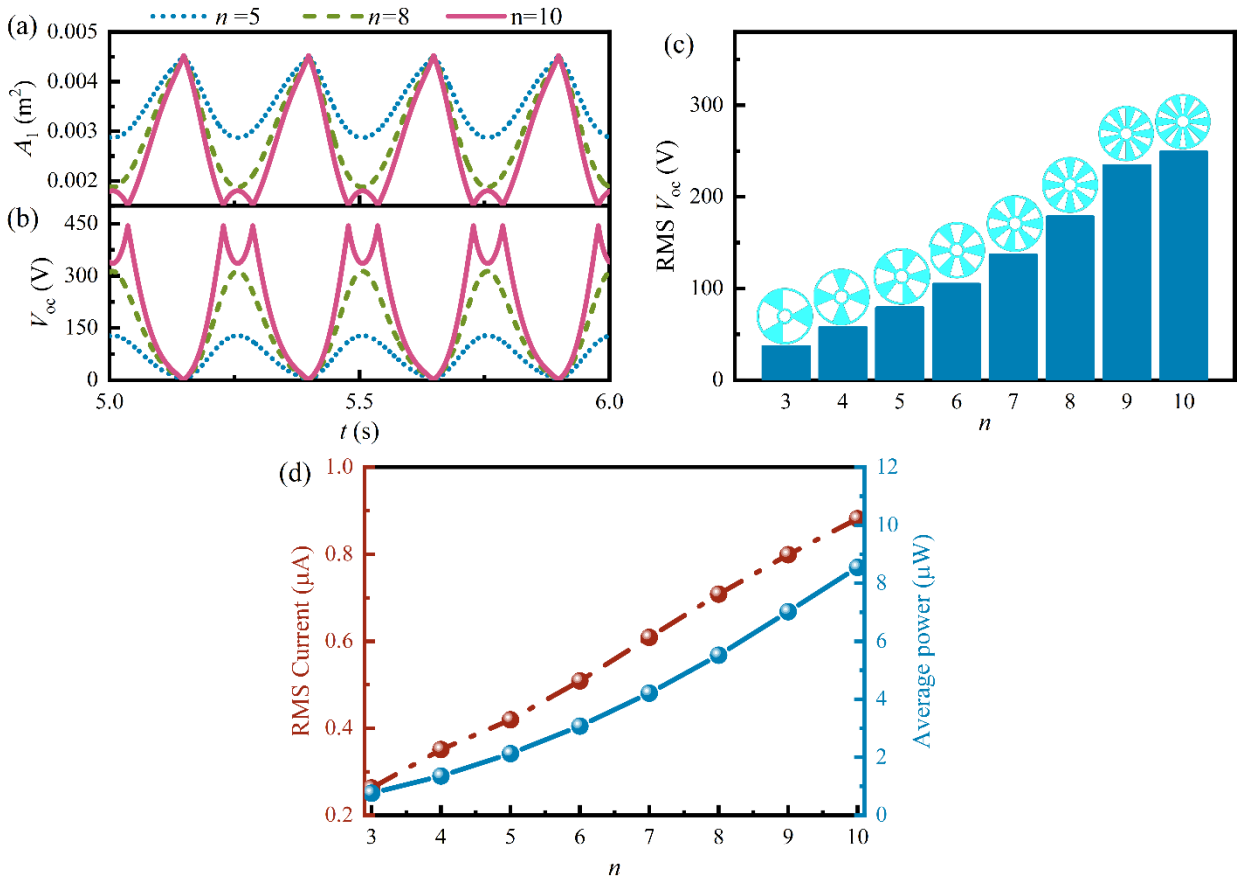


Figure 19. Effect of the sector number

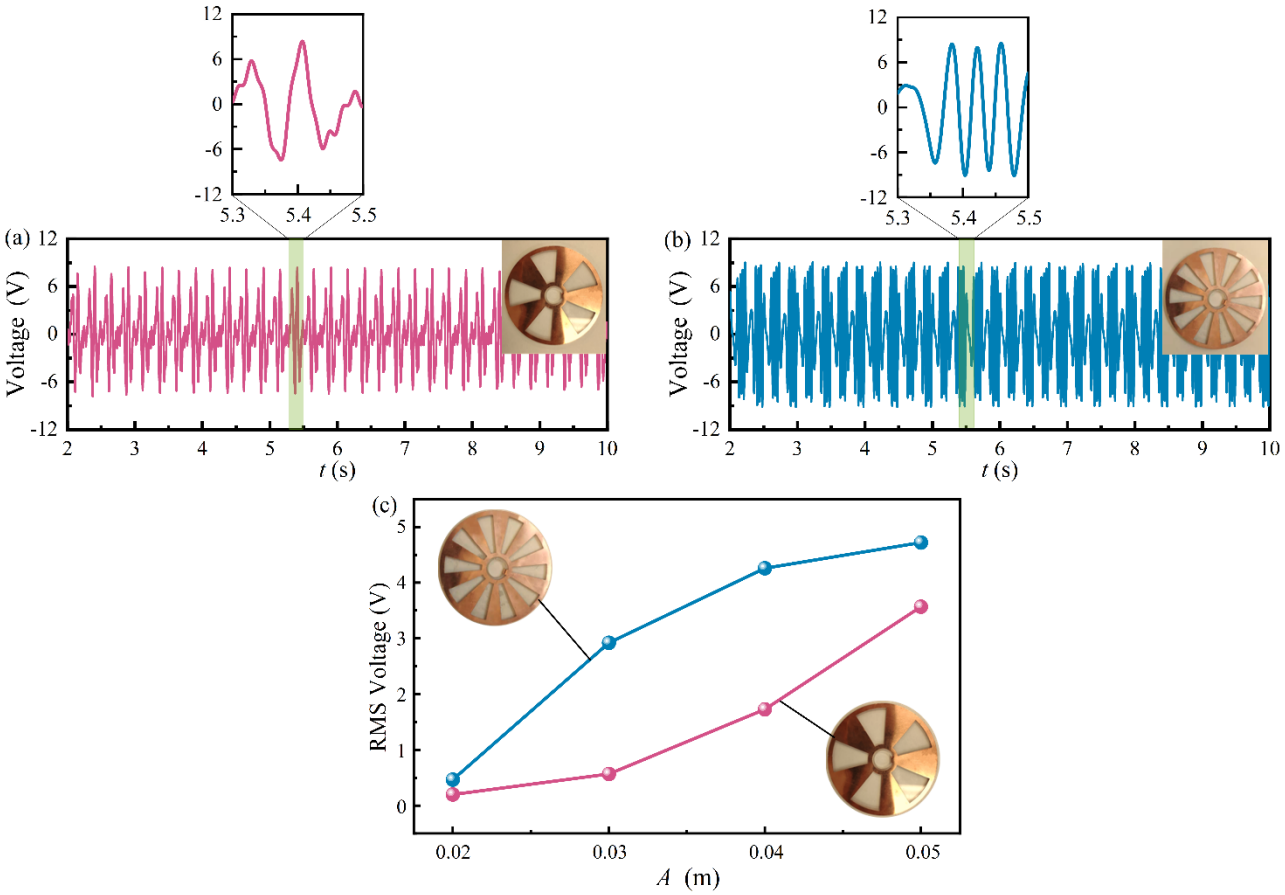


Figure 20. Experimental comparison between two different segmentation structures

## 7. Conclusions

In this paper, a disc-shaped triboelectric energy harvester is investigated for harvesting vibration energy, in which a bistable mechanism in the form of a pair of repulsive magnets is utilized. Based on the structural design, the model of the structural dynamics subjected to horizontal excitation is presented. In addition, according to the structural response, an equivalent electric model is established for modelling the electric performance of the harvester. The theoretical model of the proposed harvester is the first model linking the structural dynamics and electrical dynamics domains for disc-shaped triboelectric energy harvesters targeting vibration energy. This is the first study about a disc-shaped triboelectric energy harvester utilizing a magnetic bistable mechanism from the perspectives of structural dynamics. Both numerical simulations and experimental investigations are carried out to explore the structural dynamics behaviour and electric output characteristics. The main conclusions are drawn as follows:

(1) The comparison between the coupled and uncoupled models (with and without consideration of the electrostatic torque) indicates that the effect of the electrostatic torque between the electrodes can be neglected, which enables the structural dynamics model and electric dynamics model to be uncoupled.

(2) The effect of the magnetic bistable mechanism on the structural responses is investigated, and it is found that a slight change in the gap between the two magnets may result in distinct dynamic behaviour. The frequency bandwidth of the harvester is obviously broadened by the bistable mechanism, compared with that of the harvester without the bistable mechanism.

(3) The friction between the two discs behaves as damping during vibration in the structural dynamics of the harvester, which plays a significant role in the energy harvesting system. Interwell motion and high-periodicity oscillation are more likely to happen under a relatively low damping.

(4) The study about the basins of attraction reveals that an appropriate increase of the gap between the magnets leads to the intermingling of the basins for intrawell oscillation and interwell oscillation. A high excitation level makes the system less sensitive to the initial conditions.

(5) The experimental comparison between the harvesters with and without the bistable mechanism under different

excitation frequencies indicates that the former can achieve a higher output voltage, and increasing the amplitude of excitation improves the power of the harvester.

(6) The segmentation structure of the triboelectric films directly affects the open-circuit voltage of the harvester. The power output efficiency can be enhanced by increasing the number of the sectors on the films to a certain limit.

In the further work, some triboelectric films with high surface charge densities made by nano-scale surface texturing will be utilized in the harvester, which are excepted to significantly enhance the energy harvesting performance. Besides, based on the current design, an improved configuration with a sandwich structure consisting of two pairs of discs is under consideration, which includes two sub-harvesters that would lead to a higher efficiency.

## Acknowledgements

The first author is sponsored by a University of Liverpool and China Scholarship Council joint scholarship. The authors would also like to thank Mr Derek Neary and Mr Raymond Edun for producing the electric circuits and test rig.

## References

[1] Fan F R, Tian Z Q and Wang Z L 2012 Flexible triboelectric generator *Nano Energy* **1** 328–34

[2] Jin C, Kia D S, Jones M and Towfighian S 2016 On the contact behavior of micro-/nano-structured interface used in vertical-contact-mode triboelectric nanogenerators *Nano Energy* **27** 68–77

[3] Yang B, Zeng W, Peng Z H, Liu S R, Chen K and Tao X M 2016 A Fully Verified Theoretical Analysis of Contact-Mode Triboelectric Nanogenerators as a Wearable Power Source *Adv. Energy Mater.* **6** 1–8

[4] Niu S, Wang S, Lin L, Liu Y, Zhou Y S, Hu Y and Wang Z L 2013 Theoretical study of contact-mode triboelectric nanogenerators as an effective power source *Energy Environ. Sci.* **6** 3576–83

[5] Wang S, Lin L, Xie Y, Jing Q, Niu S and Wang Z L 2013 Sliding-triboelectric nanogenerators based on in-plane charge-separation mechanism *Nano Lett.* **13** 2226–33

[6] Niu S, Liu Y, Wang S, Lin L, Zhou Y S, Hu Y and Wang Z L 2013 Theory of sliding-mode triboelectric nanogenerators *Adv. Mater.* **25** 6184–93

[7] Meng B, Tang W, Too Z H, Zhang X, Han M, Liu W and Zhang H 2013 A transparent single-friction-surface triboelectric generator and self-powered touch sensor *Energy Environ. Sci.* **6** 3235–40

[8] Yang Y, Zhang H, Chen J, Jing Q, Zhou Y S, Wen X and Wang Z L 2013 Single-electrode-based sliding triboelectric nanogenerator for self-powered displacement vector sensor system *ACS Nano* **7** 7342–51

[9] Niu S, Liu Y, Chen X, Wang S, Zhou Y S, Lin L, Xie Y and Wang Z L 2015 Theory of freestanding triboelectric-layer-based nanogenerators *Nano Energy* **12** 760–74

[10] Jiang T, Chen X, Han C B, Tang W and Wang Z L 2015 Theoretical study of rotary freestanding triboelectric nanogenerators *Adv. Funct. Mater.* **25** 2928–38

[11] Lin L, Wang S, Xie Y, Jing Q, Niu S, Hu Y and Wang Z L 2013 Segmentally structured disk triboelectric nanogenerator for harvesting rotational mechanical energy *Nano Lett.* **13** 2916–23

[12] Lin L, Wang S, Niu S, Liu C, Xie Y and Wang Z L 2014 Noncontact free-rotating disk triboelectric nanogenerator as a sustainable energy harvester and self-powered mechanical sensor *ACS Appl. Mater. Interfaces* **6** 3031–8

[13] Jiang T, Chen X, Yang K, Han C, Tang W and Wang Z L 2016 Theoretical study on rotary-sliding disk triboelectric nanogenerators in contact and non-contact modes *Nano Res.* **9** 1057–70

[14] Kwak S S, Kim S M, Ryu H, Kim J, Khan U, Yoon H J, Jeong Y H and Kim S W 2019 Butylated melamine formaldehyde as a durable and highly positive friction layer for stable, high output triboelectric nanogenerators *Energy Environ. Sci.* **12** 3156–63

[15] Tao K, Wang B, Chen Y, Tang L, Wu J and Chang H 2019 Bipolar Micro Electret Power Generator *32nd International Conference on Micro Electro Mechanical Systems (MEMS)*

[16] Zhang Z, Bai Y, Xu L, Zhao M, Shi M, Wang Z L and Lu X 2019 Triboelectric nanogenerators with simultaneous outputs in both single-electrode mode and freestanding-triboelectric-layer mode *Nano Energy* **66**

[17] Wang J, Ding W, Pan L, Wu C, Yu H, Yang L, Liao R and Wang Z L 2018 Self-Powered Wind Sensor System for Detecting Wind Speed and Direction Based on a Triboelectric Nanogenerator *ACS Nano* **12** 3954–63

[18] Lin Z, Zhang B, Zou H, Wu Z, Guo H, Zhang Y, Yang J and Wang Z L 2020 Rationally designed rotation triboelectric nanogenerators with much extended lifetime and durability *Nano Energy* **68** 104378

[19] Wang J, Meng C, Gu Q, Tseng M C, Tang S T, Kwok H S, Cheng J and Zi Y 2020 Normally Transparent Tribo-Induced Smart Window *ACS Nano* **14** 3630–9

[20] Bai Y, Xu L, He C, Zhu L, Yang X, Jiang T, Nie J, Zhong W and Wang Z L 2019 High-performance triboelectric nanogenerators for self-powered, in-situ and real-time water quality mapping *Nano Energy* **66** 104117

[21] Zhu G, Chen J, Zhang T, Jing Q and Wang Z L 2014 Radial-arrayed rotary electrification for high performance triboelectric generator *Nat. Commun.* **5**

1–9

[22] Singh H H and Khare N 2019 Improved performance of ferroelectric nanocomposite flexible film based triboelectric nanogenerator by controlling surface morphology, polarizability, and hydrophobicity *Energy* **178** 765–71

[23] Bhatta T, Maharjan P, Cho H, Park C, Yoon S H, Sharma S, Salauddin M, Rahman M T, Rana S S and Park J Y 2021 High-performance triboelectric nanogenerator based on MXene functionalized polyvinylidene fluoride composite nanofibers *Nano Energy* **81** 105670

[24] Mutlu S, Unlu K, Gevrek T N and Sanyal A 2020 Expanding the versatility of poly(dimethylsiloxane) through polymeric modification: An effective approach for improving triboelectric energy harvesting performance *Smart Mater. Struct.* **29**

[25] Nafari A and Sodano H A 2018 Surface morphology effects in a vibration based triboelectric energy harvester *Smart Mater. Struct.* **27**

[26] Fan F, Lin L, Zhu G, Wu W, Zhang R and Wang Z L 2012 Transparent Triboelectric Nanogenerators and Self-Powered Pressure Sensors Based on Micropatterned Plastic Films *Nano Lett.* **12** 3109–3114

[27] Dhakar L, Tay F E H and Lee C 2015 Development of a broadband triboelectric energy harvester with SU-8 micropillars *J. Microelectromechanical Syst.* **24** 91–9

[28] Zhai C, Chou X, He J, Song L, Zhang Z, Wen T, Tian Z, Chen X, Zhang W, Niu Z and Xue C 2018 An electrostatic discharge based needle-to-needle booster for dramatic performance enhancement of triboelectric nanogenerators *Appl. Energy* **231** 1346–53

[29] Elvin N and Erturk A 2013 *Advances In Energy Harvesting Methods* (Springer)

[30] Li Y, Zhou S, Yang Z, Guo T and Mei X 2019 High-performance low-frequency bistable vibration energy harvesting plate with tip mass blocks *Energy* **180** 737–50

[31] Mei X, Zhou S, Yang Z, Kaizuka T and Nakano K 2021 Enhancing energy harvesting in low-frequency rotational motion by a quad-stable energy harvester with time-varying potential wells *Mech. Syst. Signal Process.* **148** 107167

[32] Costa L G, Monteiro L L da S, Pacheco P M C L and Savi M A 2020 A parametric analysis of the nonlinear dynamics of bistable vibration-based piezoelectric energy harvesters *J. Intell. Mater. Syst. Struct.* **32** 699–723

[33] Huang X and Yang B 2021 Improving energy harvesting from impulsive excitations by a nonlinear tunable bistable energy harvester *Mech. Syst. Signal Process.* **158** 107797

[34] Yu N, Ma H, Wu C, Yu G and Yan B 2021 Modeling and experimental investigation of a novel bistable two-degree-of-freedom electromagnetic energy harvester *Mech. Syst. Signal Process.* **156**

[35] Abdelnaby M A and Arafa M 2020 A bistable electromagnetic energy harvester for low-frequency, low-amplitude excitation *J. Brazilian Soc. Mech. Sci. Eng.* **42**

[36] Nelson D, Ibrahim A and Towfighian S 2019 Sensors and Actuators A : Physical Dynamics of a threshold shock sensor : Combining bi-stability and triboelectricity *Sensors Actuators A. Phys.* **285** 666–75

[37] Fu Y, Ouyang H and Benjamin Davis R 2020 Nonlinear structural dynamics of a new sliding-mode triboelectric energy harvester with multistability *Nonlinear Dyn.* **1**–**22**

[38] Fu Y, Ouyang H and Davis R B Effects of electrical properties on vibrations via electromechanical coupling in triboelectric energy harvesting *J. Phys. D. Appl. Phys.* 1–24

[39] Micro-actuator B 2018 Toward Self-Control Systems for Neurogenic Underactive Bladder : A Triboelectric Nanogenerator Sensor Integrated with a Bistable Micro-Actuator *ACS Nano* **12** 3487–501

[40] Deng H, Ye J, Du Y, Zhang J, Ma M and Zhong X 2019 Bistable broadband hybrid generator for ultralow-frequency rectilinear motion *Nano Energy* **65** 1–9

[41] Harne R L and Wang K W 2013 A review of the recent research on vibration energy harvesting via bistable systems *Smart Mater. Struct.* **22**

[42] Brennan R R M J and Kovacic B R M I 2010 Potential benefits of a non-linear stiffness in an energy harvesting device *Nonlinear Dyn.* 545–58

[43] Fang H and Wang K W 2017 Piezoelectric vibration-driven locomotion systems – Exploiting resonance and bistable dynamics *J. Sound Vib.* **391** 153–69

[44] Huguet T, Lallart M, Badel A, Huguet T, Lallart M and Badel A 2019 Orbit jump in bistable energy harvesters through buckling level modification *Mech. Syst. Signal Process.* **128** 202–15

[45] Yung K W, Landecker P B and Villani D D 1998 An Analytic Solution for the Force Between Two Magnetic Dipoles *Magn. Electr. Sep.* **9** 39–52

[46] Wang Y, Gao M, Ouyang H, Li S, He Q and Wang P 2020 Modelling, simulation, and experimental verification of a pendulum-flywheel vibrational energy harvester *Smart Mater. Struct.* **29**

[47] Zhang C and Wang Z L 2016 *Triboelectric Nanogenerators*

[48] Tao K, Lye S W, Miao J, Tang L and Hu X 2015 Out-of-plane electret-based MEMS energy harvester with the combined nonlinear effect from electrostatic force and a mechanical elastic stopper *J. Micromechanics Microengineering* **25** 104014

[49] Boisseau S, Despesse G and Ahmed B 2012 Electrostatic Conversion for Vibration Energy Harvesting *Small-Scale Energy Harvest.* 1–39

[50] Fu Y, Ouyang H and Davis R B 2019 Triboelectric energy harvesting from the vibro-impact of three

cantilevered beams *Mech. Syst. Signal Process.* **121** 509–31

[51] Diaz A F and Felix-Navarro R M 2004 A semi-quantitative tribo-electric series for polymeric materials: The influence of chemical structure and properties *J. Electrostat.* **62** 277–90

[52] Berger E J 2002 Friction modeling for dynamic system simulation *Appl. Mech. Rev.* **55** 535–77

[53] Popp.K and Stelter.P 1990 Stick-slip vibrations and chaos *Philos. Trans. R. Soc. London. Ser. A Phys. Eng. Sci.* **332** 89–105